Cellulose
https://doi.org/10.1007/s10570-018-1739-x

ORIGINAL PAPER

Dispersing and stabilizing cellulose nanoparticles in acrylic resin dispersions with unreduced transparency and changed rheological property

Lanxing Du · Tuhua Zhong · Michael P. Wolcott · Yang Zhang · Chusheng Qi · Boshi Zhao · Jinwu Wang · Zhiming Yu

Received: 20 August 2017 / Accepted: 6 March 2018

Abstract This paper evaluates the potential of using 2,2,6,6-tetramethylpiperidin-1-yl)oxyl (TEMPO)-oxidized cellulose nanoparticles (T-CNPs) as additives to tune the rheology of water-based acrylic resin (AR) coatings for flexible packaging applications. Three T-CNPs of T-CNF, T-MCC, and T-CNC were prepared from three starting cellulosic materials: cellulose nanofibers (CNF), microcrystalline cellulose (MCC), and cellulose nanocrystals (CNC), respectively. Their sizes ranged from 20 nm to 20 μm in diameter, and 234 nm to over 500 nm in length. The oxidation imparted carboxyl groups on the surfaces of nanoparticles ranging from 1.99 to 2.79 mmol/g and increased the zeta-potentials of the nanoparticles, clearly improving the dispersibility and stability of the CNPs in AR. The AR/T-CNP dispersion showed unreduced transparency. The morphologies of the T-CNPs affected the rheological properties of the AR/T-CNP dispersions. The larger aspect ratio of T-CNF and T-MCC resulted in the high viscosity and solid-like viscoelastic behavior of the AR/nanoparticle dispersions at a concentration of 0.78 wt%. The CNC and T-CNC with a smaller particle size and aspect ratio had less effect on the viscosity and rheological behavior of the resulting dispersions compared with the others—even at a high content of 1.30 wt%. Due to a lower aspect ratio but a relatively large particle size, the AR/T-MCC dispersions exhibited elastic gel-like rheological properties at a low content.

Keywords Cellulose nanoparticles · TEMPO-oxidation · Acrylic resin · Aspect ratio · Transparency · Rheological property

L. Du · Y. Zhang · C. Qi · B. Zhao · Z. Yu (✉)
College of Material Science and Technology, Beijing Forestry University, Beijing 100083, China
e-mail: yuzhiming@bjfu.edu.cn

L. Du · T. Zhong · M. P. Wolcott
Composite Materials and Engineering Center, Washington State University, Pullman, WA 99163, USA

J. Wang (✉)
Forest Products Laboratory, US Forest Service, Madison, WI 53726, USA
e-mail: jinwuwang@fs.fed.us

Introduction

Owing to low emission of volatile organic chemicals, water-based acrylic resins are gradually replacing solvent-based resins (Elrebii et al. 2014; Duan et al. 2017). They can be applied in food packaging. Films coated by this acrylic resin are utilized for direct product overwrap or carton overwrap applied in the bakery, biscuit, and confectionery industries, where gas barrier and optimum product presentation is required. However, water-based acrylic resins are not satisfied in a gas barrier. Sanchez-Garcia and Lagaron (2010) prepared a cellulose/PLA film and

Published online: 10 March 2018

indicated that cellulose or their derivatives can serve as additives in coatings to improve the oxygen barrier properties and the mechanical properties of packaging films. Therefore, depending on the barrier theory, water-based acrylic resin/cellulose nanoparticles (CNPs) was developed.

A significant amount of work has been done to physically add cellulose nanoparticles (CNPs) in the water-based acrylic resin system. The resultant coatings present improved hardness, Young's modulus, tensile strength, scratch resistance, as well as a lower gloss (Veigel et al. 2014). This was attributable to the inhomogeneous dispersion and instability of cellulose nanofibers (CNFs) in acrylic resins. To improve the light property and dispersion, γ-aminopropyltriethoxysilane was employed (Tan et al. 2016). Ester bonds formation regenerates the chemical cross-linking and steric hindrance influence, helping stabilize the CNFs in acrylic resin. However, it requires high energy consumption in the physical preparation of CNPs, and extra process and chemical agent in preparation of CNP/acrylic resin. A facile and effective way to enhance the dispersion of CNPs in water-based acrylic resin is essential. 2,2,6,6-Tetramethylpiperidin-1-yl)oxyl (TEMPO)-mediated oxidation is a promising approach. This oxidation not only reduces the particle size of CNPs and improves the transparency of CNP dispersions, but also imparts sufficient negative charges on CNPs, resulting in the CNPs almost completely dispersing individually in aqueous media, even the acrylic resin (Okita et al. 2010; Shinoda et al. 2012; Baldacchini et al. 2004). This is because acrylic resin commonly used for commercial purposes are negatively charged. It is theoretically assumed that the oxidized CNP and acrylic resin mutually repulse, leading to the maintenance of good stability and dispersion. The design for oxidized cellulose/acrylic resin is both reasonable and feasible.

In the cellulose/acrylate system, rheological property is a key factor influencing the subsequent coating. It has been proven that nanofibrillated cellulose obtained by physical treatment is able to change the rheological properties of pure acrylate polymer (Grüneberger et al. 2014). Similar behavior appeared in cellulose nanocrystal/epoxy polymer emulsion, and nanofibrillated cellulose/kaolin clay/carboxylated styrene-butadiene latex (Ruiz et al. 2001; Bousfield et al. 2013). Researchers consider this characteristic behavior resulting from the features of cellulose suspension, intrinsically the features of the CNPs—particle size, aspect ratio (length to diameter, L/d), surface functional groups, and concentrations (Grüneberger et al. 2014; Li et al. 2015). Concentrated cellulose suspension significantly exhibits pseudoplastic fluid properties (Boluk et al. 2012). An enlargement in length and L/d of cellulose nanofibrils (CNFs) lead to cellulose dispersions showing a high viscosity (Benhamou et al. 2014). The suspension of cellulose derivatives also presents different viscosity and rheological behavior (Moberg et al. 2017). However, no available study concretely evaluates the physical structural features on influencing the rheological behaviors of the cellulose/polymer system, which affects the flowability in future coating and properties of the resulting film.

Therefore, the objective of this study is to use a TEMPO-mediated oxidation system to decorate negatively charged carboxyl group on cellulose, providing repulsive forces among acrylic macromolecues and cellulose nanoparticles, leading to improvements in the dispersity and stability of cellulose nanoparticles in acrylic solution. Furthermore, the study also investigated the physical structural features of cellulose nanoparticles and the content in dispersions affecting the rheological properties of the resultant cellulose/acrylic dispersions. It is expected that this knowledge will help design their applications in coatings and films.

Materials and methods

Raw materials

Cellulose nanocrystals (CNCs, slurry, ~ 11.8% solids) were made by the U.S. Forest Service Forest Products Laboratory and cellulose nanofibrils (CNFs, slurry, 2.8% solids) were made by the University of Maine, ME, USA. Acrylic resin (AR, Joncryl 678) was provided by BASF Co. Joncryl 678 is a styrene-acrylic acid copolymer with a molecular weight of 8600 and an acid number of 215. Microcrystalline cellulose (MCC), TEMPO, sodium bromide (NaBr), sodium hypochlorite (NaClO) in solution (10–15%), ammonia hydroxide (28%), and other chemicals were purchased from Sigma-Aldrich Inc., USA.

Preparation of T-CNPs

Each type of cellulose (1 g, solid) was suspended in deionized water (50–100 mL) with a mixture of TEMPO (0.016 g) and NaBr (0.1 g). The TEMPO oxidation began by slowly adding NaClO (10 mmol/g cellulose). This mixed suspension was continuously stirred at room temperature and kept in an alkaline environment (pH = 10.5 ± 0.2) by the addition of 0.5 M NaOH. Since CNF, MCC, and CNC had different processing histories, it took 7, 9, and 21 h, respectively, for sufficient oxidation to occur until the consumption of NaOH had ceased—as indicated by the disappearance of the yellow color, which was a result of the generation of free chlorine during the oxidation process. The CNC were prepared by the concentrated sulfuric acid, resulting in sulfate ester groups on the surface of cellulose nanoparticles, which might hinder the TEMPO oxidation. On the contrary, the CNF were prepared by mechanical defibrillation with more hydroxyl groups, which might be easier to be oxidized. The MCC had been subject to more chemical treatments than the CNF, and hence it took more time. Ethanol (2–5 mL/g cellulose) was then added to terminate the reaction. The resulting suspension was adjusted to pH = 7 by adding 0.5 M HCl, dialyzed, and centrifuged at 15,000 rpm. The neutral oxidized CNP slurries were collected and labeled as T-CNFs, T-MCC, and T-CNCs (collectively, TEMPO-oxidized cellulose nanoparticles, T-CNPs) prepared from the starting cellulose of CNFs, MCC, and CNCs, respectively.

Preparation of AR/T-CNP dispersions

The AR/T-CNP dispersions comprised of 26 wt% of solid acrylic powder, 6.3 wt% of $NH_3{\cdot}H_2O$ (28 wt%), and 67.7 wt% of various concentrated CNP dispersions. The CNC or T-CNP dispersions with various concentrations were prepared by adding deionized water; following these dispersions, they were then sonicated (amplitude 15%, Branson 5510, USA) until the cellulose uniformly dispersed (Table 1). These mixtures were stirred at room temperature until the AR/T-CNP or AR/CNC dispersions became completely transparent.

FTIR

Fourier transform infrared spectroscopy (Nicolet iS50 FT-IR, Thermo Nicolet, USA) was used to determine the functional groups in the CNPs and the T-CNPs. All suspensions (including CNF, CNC, T-CNF, T-MCC, and T-CNC) except MCC were diluted to 0.1% (w/v) using deionized water. KBr (200 mg) was dissolved in these diluted suspensions (2 mL) by adding 0.5 M HCl solution until the pH = 2–3. The mixture was sonicated for 1 min to complete the dilution. MCC was mixed with KBr at a ratio of 1:100. The mixed suspensions and the powder were completely oven-dried at 40 °C. The dried samples were ground and pressed into transparent pellets, and were analyzed in transmittance mode within a range of 500–3700 cm^{-1}.

Titration

An electric conductivity titration method was used to perform the determination of the carboxylate group content of the T-CNPs (Saito and Isogai, 2004). Briefly, the freeze-dried samples (0.3 g) were dispersed in deionized water (55 mL), followed by the addition of 0.01 M HCl (5 mL). The mixture underwent sonication for 2 min and the pH value was adjusted to 2–3 by adding 0.1 M HCl. Subsequently, the pH value was adjusted to 11 by adding 0.04 M NaOH at a rate of 0.1 mL/min. The relationship of conductivity and pH was recorded and used to calculate the carboxylate content of the samples. The carboxyl group was calculated as the following equation:

$$Carboxyl\ group\ content = \frac{c \times Mw \times V}{Mw \times m} \quad (1)$$

where c is the molality of NaOH, 0.04 M, mol/L; Mw is the molar weight of NaOH; V is the titration volume of 0.04 M NaOH solution, mL; and m is the weight of cellulose, g.

TEM and SEM

The CNC, CNF, T-CNF, T-MCC, and T-CNC dispersions were adjusted to 0.01% (w/v) and followed by sonication for 10 min. A 5-μL droplet of the dispersions was deposited on a formvar- and carbon-coated copper grid and was stained with 1 wt% uranyl acetate for 30 min before it was completely dried. The dried

Table 1 The formula of AR/T-CNP dispersions

Dispersions	Effective components (total 100 g)			Cellulose concentration based on AR (wt%)
	AR(solid) (g)	$NH_3{\cdot}H_2O$ (28%) (g)	Cellulose (solid) (g)	
AR/T-CNF, AR/T-MCC	26	6.3	0.26, 0.52, 0.78	1, 2, 3
AR/T-CNC, AR/CNC	26	6.3	0.26, 0.52, 0.78, 1.04, 1.30	1, 2, 3, 4, 5

sample grid was evaluated using a transmission electron microscope (TEM) (JEOL 1200 EX, TEOL, Tokyo, Japan) with an accelerating voltage of 5 kV. The oven-dried MCC were fixed on carbon adhesive disks and sputter-coated with platinum with a thickness of 2.8 nm. The MCC was observed with a scanning electron microscope (SEM) (FEI SEM Quanta 200F, FEI Company, OR, USA) with an accelerating voltage of 5 kV. The particle size and L/d measurements of the samples were based on 100 individual particles selected from the TEM and SEM images and analyzed by using ImageJ software (Du et al. 2017).

XRD

The X-ray diffraction (XRD) patterns of 6 samples were measured by using a Rigaku Miniflex 600 X-ray diffractometer (Rigaku Corporation, Tokyo, Japan) operated at a Ni-filtered Cu Kα radiation (λ = 0.15418 Å) with 45 kV and 40 mA in a 2θ range of 10° to 40° at a step size of 0.02. The crystalline index (CrI) for the samples was calculated with the following equation (Kargarzadeh et al. 2012):

$$Cr\ (\%) = (I_{Max} - I_{Am})/I_{Max} \times 100 \quad (2)$$

where I_{Max} is the maximum intensity of the principal peak and I_{Am} is the intensity of the diffraction attributed to the amorphous cellulose.

Zeta potential

A Malvern 3000 Zetasizer Nano ZS (Malvern Instruments Ltd., Worcestershire, UK) was used to determine the electrophoretic mobility of the starting materials and the T-CNP dispersions at a concentration of 0.005 wt%. The detecting angle was 173° and the wavelength was 633 nm. The zeta potential is calculated as follows:

$$U_E = \frac{2\varepsilon z f(ka)}{3\eta} \quad (3)$$

where U_E is the electrophoretic mobility, ε is the dielectric constant, z is the zeta potential, f(ka) is Henry's function, and η is the viscosity (Hunter 1981).

Visual inspection of stability and UV/VIS spectrometer

Ten grams of the T-CNP dispersions, prepared AR/T-CNPs, or starting materials with AR dispersions were added into 20-mL vials. The stability was visually checked after storage at 0, 1, and 30 days at room temperature. To obtain light transmittance, the samples were scanned from 400 to 800 nm at a 1-nm step using a Lambda 25 UV/VIS spectrometer (PerkinElmer, USA). The spectrum of a cuvette filled with deionized water was used as a reference to correct the transmittance of the dispersions. The absorption of the dispersions was obtained at 600 nm wavelengths for comparison.

Rheological measurements

The rheological properties of the freshly-prepared T-CNPs and the resulting dispersions stored for 1 day were analyzed using an MCR 302 rheometer (Anton Paar GmbH, Graz, Austria) equipped with a cone-and-plate geometry (50 mm diameter parallel plate, PC50-1, with a gap fixed at 0.01 mm and a cone angle of 1°). The rheological measurements were conducted at 25 °C. The steady-shear viscosity was tested with a shear rate ranging from 0.1 to 1000 s^{-1}. Frequency sweep tests ranging from 1 to 100 s^{-1} were conducted with a strain of 0.1%.

Results and discussion

Chemical characterization

The TEMPO-mediated oxidation converted some hydroxyl groups on the surface of the CNPs into the carboxyl groups, exhibiting two narrow and weak absorption peaks and an increase in the absorption feature (Fig. 1). The sharp and weak absorption bands at 3420 and 2910 cm^{-1} were attributed to O–H stretching and asymmetric C–H stretching, indicating that the TEMPO-mediated oxidation caused the reduction of the hydroxyl groups and the breakage of the cellulose chains (Shibata and Isogai 2003). Since the samples were prepared at pH = 2 ~ 3, the protonated carboxylic acid yield absorption bands on cellulose were exhibited. The carbonyl stretch (C=O) appeared between 1738 and 1748 cm^{-1}, and C–O–H vibrations were observed between 1200 and 1300 cm^{-1} (Hay and Myneni 2007).

Figure 2 shows that the carboxylate content of the T-CNPs differed owing to the different conditions of the cellulose surface. The T-CNCs only contained 1.99 mmol/g carboxylate groups, resulting from the esterification between cellulose and sulfate groups that occurred during the preparation of the CNCs. The ester groups had been introduced on the partial of C2, C3, and C6 sites of the CNCs during their preparation; some of these sulfate groups might be removed and

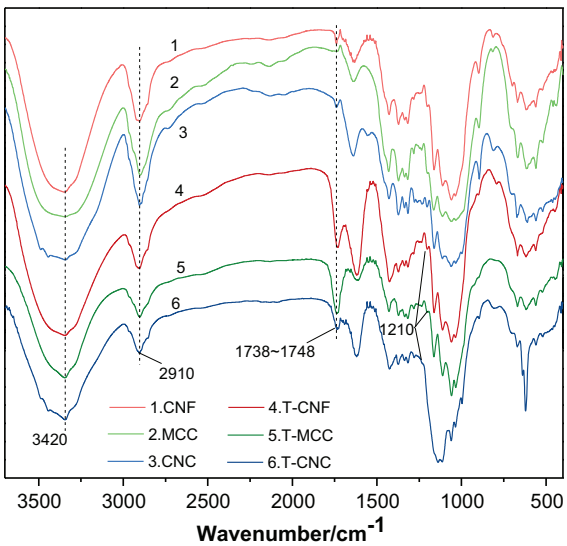

Fig. 1 FTIR spectrum of the CNPs and the resulting T-CNPs

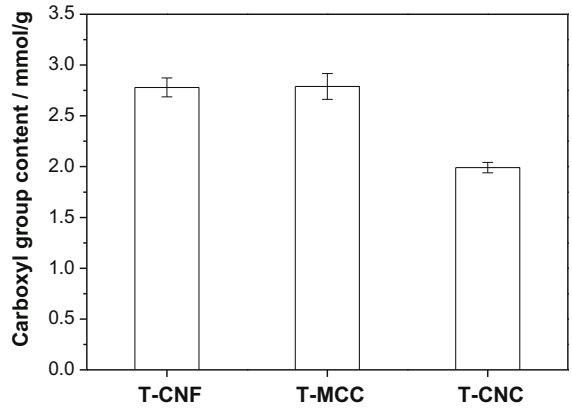

Fig. 2 The carboxyl group contents of the T-CNPs

substituted by carboxyl groups during the TEMPO-mediated oxidation. CNF had more exposed surface per gram to the oxidation than MCC, it was assumed that CNF had high carboxylate content, while the T-CNFs and T-MCC had similar carboxylate contents, 2.78 and 2.79 mmol/g cellulose, respectively—even the T-MCC had a slightly higher carboxylate content. This might be attributed to the very large L/d of the CNFs causing the aggregation by the strong hydrogen bond and hindering the TEMPO oxidation. However, the NaClO was consumed due to the increase in oxidizing time and the dispersion of the CNF. MCC exposed more area with the reduction of particle size caused by the increasing oxidation time. These resulted in an equal amount of carboxylate for T-CNF and T-MCC.

Crystallinity and structure

Figure 3 shows the XRD patterns and crystallinity indices of the starting cellulose samples and the T-CNPs. The diffraction peaks at around 15.6°, 17°, and 22.7° correspond to the cellulose I crystal form (French 2014). The patterns of the resulting CNPs were unchanged, implying that the TEMPO oxidation did not alter the crystalline structure I of the starting samples (Lin et al. 2013). However, a decrease was observed in the diffraction intensity of the feature peaks diffracted by the oxidized CNPs (T-CNF, T-MCC, and T-CNC, respectively), which was consistent with the decrease in the crystallinity indices from 64.5, 81, and 84.3% to 62.5, 77.4, and 79.4%, respectively. The reduction suggested that the

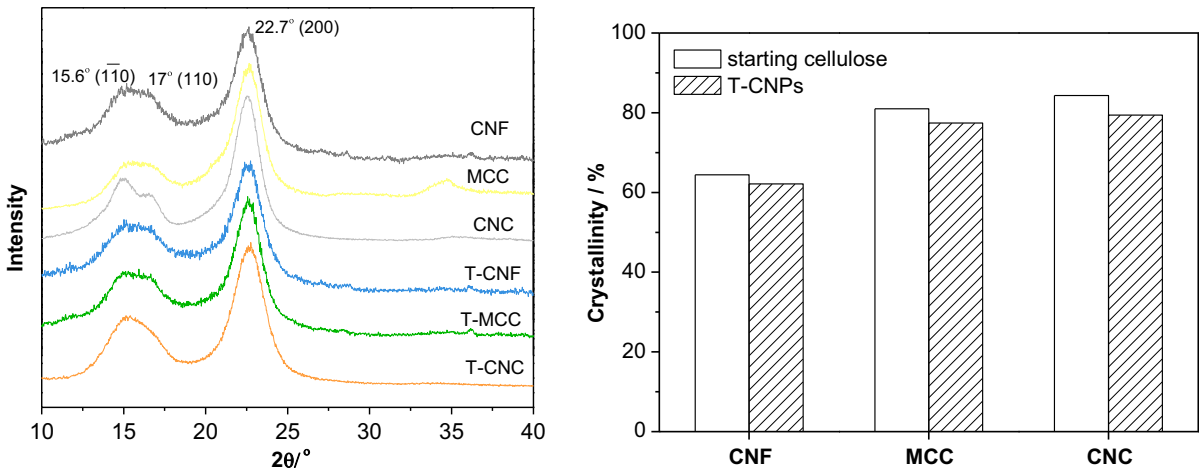

Fig. 3 The diffraction patterns and crystallinity of the CNPs and the T-CNPs

oxidizing reagents were able to penetrate the crystals and partially destroy the crystalline structure (Feng and Hsieh 2013). Therefore, the MCC—and even the CNCs with high crystallinity—exhibits a clear decrease in the crystallinity. The remaining lignin and hemicellulose covered the surfaces of the CNFs (Li et al. 2015), potentially hindering oxidation and resulting in a smaller reduction compared to the other oxidized CNPs.

The morphology, particle size, and $\overline{L}/d$ of the CNF, MCC, CNC and T-CNPs are shown in Figs. 4, 5 and Table 2. A different size reduction in the longitudinal direction and the cross section was observed between the starting cellulose samples and the T-CNPs. Individual nanofibers with lengths greater than 500 nm were observed (Fig. 4a). Owing to the considerable agglomeration of the nanofibers with few straight fibers, it was very difficult to calculate the lengths and the L/d of the original CNFs. The T-CNFs had a very long, needle-like shape. Their length and L/d values covered a large range that was greater than the range for the T-MCCs and T-CNCs. The CNCs appeared to be bundle-like in shape consisting of multiple parallel nanocrystalline fibrils (Fig. 4c). Their sizes were already in nano-scale dimensions and the distribution of L/d is left-skewed in the range of 1–37 (Fig. 5 CNC). The TEMPO oxidation changed the surface functionality of the CNCs and reduced the bundled fibrils of the CNCs into individual fibrils of the resulting T-CNCs whose L/d was nearly twice as

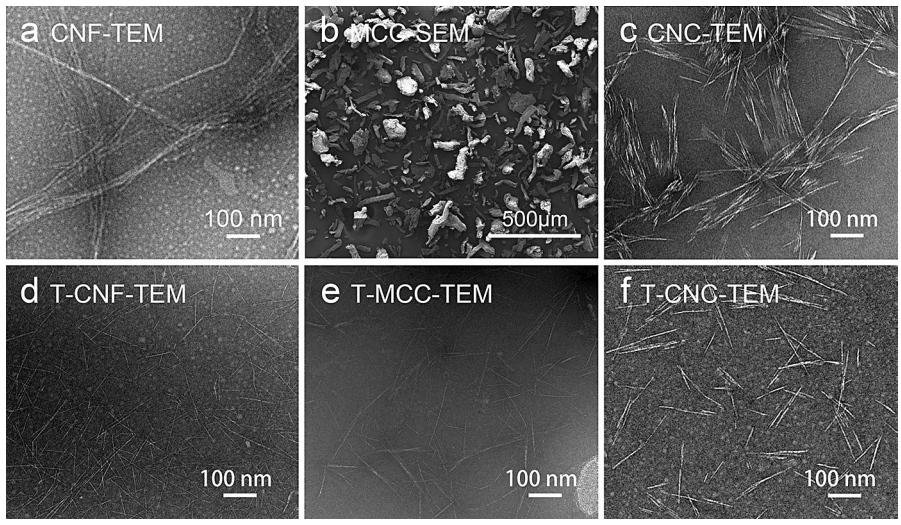

Fig. 4 Morphology of CNF, MCC, CNC and their T-CNPs (**a** CNF; **b** MCC; **c** CNC; **d** T-CNF; **e** T-MCC; **f** T-CNC)

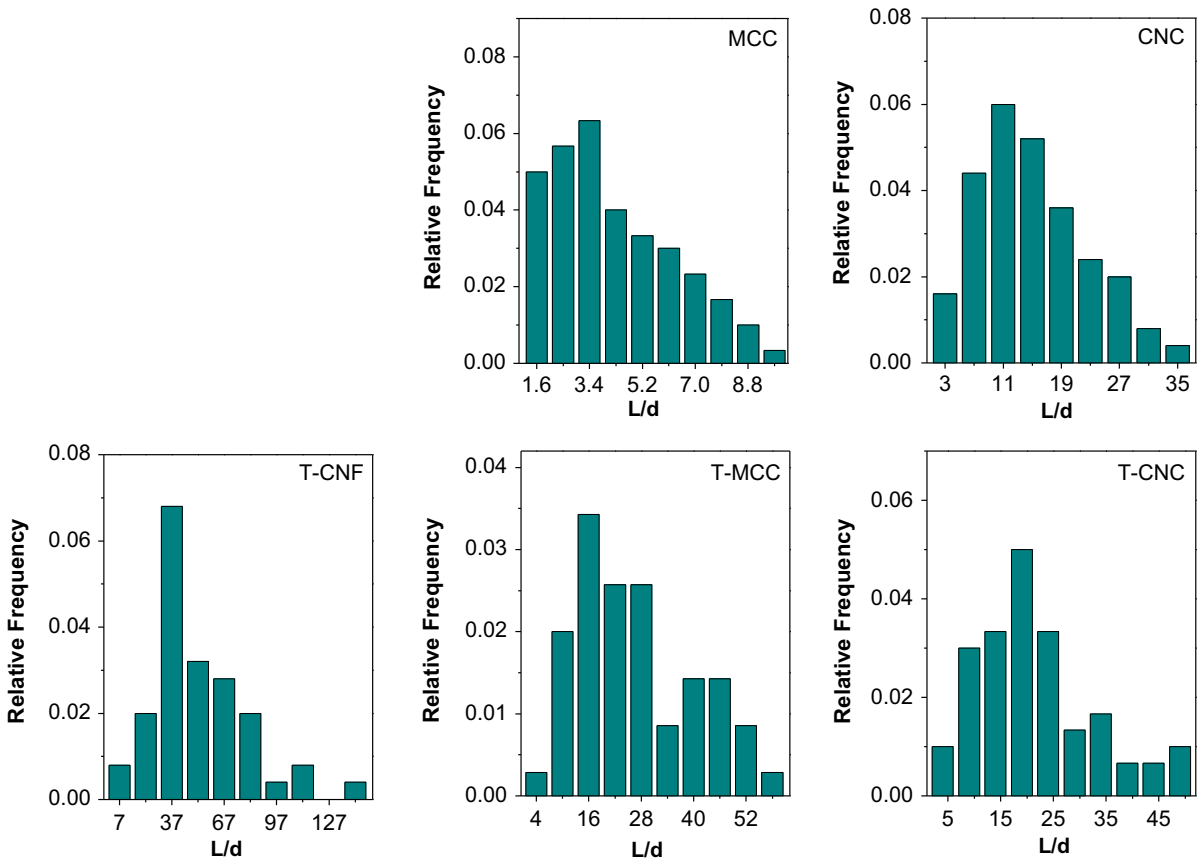

Fig. 5 The $\overline{L}/d$ distributions of the CNF, MCC, CNC, and T-CNPs

Table 2 Particle sizes of CNPs and T-CNPs

Samples	Length	Diameter	Samples	Length (nm)	Diameter (nm)
CNF	> 500 nm	26 (19) nm	T-CNF	174 (88)	3.6 (1.3)
MCC	74 (42) μm	20 (10) μm	T-MCC	149 (83)	6.5 (5.4)
CNC	234 (119) nm	20 (9) nm	T-CNC	108 (60)	5.9 (3.0)

The values in brackets are standard deviations

large as that of the starting CNCs (Fig. 4f, Table 2). As a result, the T-CNCs were better dispersed and more stable in aqueous media than the CNCs. Different from the original CNFs and CNCs, the MCCs had micro-scale dimensions, which is mostly elliptic in shape with a narrow distributed L/d ranging from 1 to 9.6. The resulting T-MCCs were reduced to nanocrystals after the oxidation, having a length being hundreds of times smaller, having a higher L/d aspect ratio, and exhibiting a wider distribution than the MCC. This reveals that the TEMPO oxidation effectively reduced the length more than the lateral dimension. These results show no matter what the starting particle size is, the TEMPO oxidation can reduce the particles to nanoscale.

The visual stability and transparency of the CNP dispersions and the AR/T-CNPs dispersions

Figure 6a shows the light transmittance of the T-CNP dispersions and the same samples that were ultrasonically treated in the visible wavelength range of

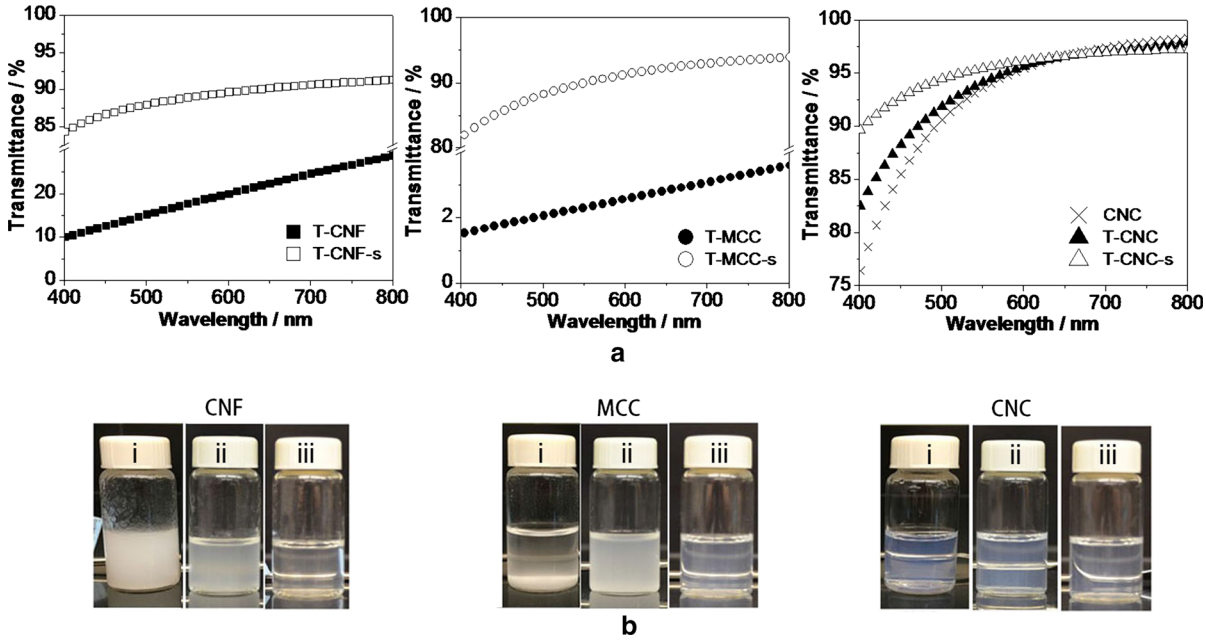

Fig. 6 Transparency of the T-CNPs and the resulting ultrasonically treated CNP dispersions with a concentration of 0.5 wt% (**a**); visual observations (**b**). s refers to ultrasonic treatment; the starting cellulose (i); T-CNP suspensions without sonication (ii); T-CNP suspensions with sonication (iii)

400–800 nm. It was expected that the aggregation of CNFs led to light being hindered by CNF, and heavy weight of MCC with low L/d resulted in MCC be deposited at the bottom of the media (Fig. 6b), respectively. The CNC dispersion had a good transmittance due to excellent dispersibility and small particle size; a transmittance of 95% at 600 nm wavelength was observed. As the resulting T-CNPs had diameters smaller than the wavelength of visible light (Jin et al. 2014), light was able to bypass T-CNPs, and the suspensions of T-CNF, MCC, and CNC dispersions, exhibited high transmittance values of 90, 93, and 97% at 600 nm wavelength, respectively. Moreover, the addition of T-CNP in acrylic resin hardly affected the transparency of the original acrylic resin; the transmittance of AR/T-CNP dispersions was all in a range of 88–90% at wavelength range from 400 to 800 nm (Fig. 7). It resulted from the limitation of T-CNP concentration and the nano-scale dimension (Tan et al. 2016).

Three transparent or translucent gel-like dispersions with different T-CNPs are shown in Fig. 8. The dispersions were well dispersed and stabilized suitably in the acrylic resin even after 30 days, promising their storage ability and implying that the CNPs and the

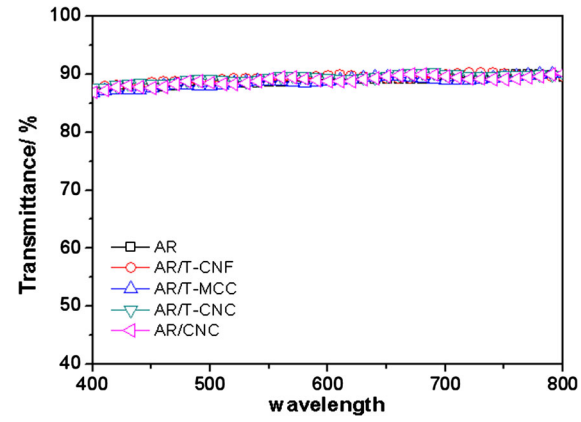

Fig. 7 Transparency of the AR/T-CNP dispersions with a T-CNP concentration of 0.78 wt%

acrylic resin exhibited good compatibility. Both acrylic resin and oxidized cellulose contained carboxylic acid groups on the surface of the molecular chain. This not only facilitated the compatibility of the biphasic dispersions but also provided the repulsive force for forming the homogeneous dispersions (Fig. 8a). The CNF dispersions were ultrasonically treated to achieve homogeneity with the acrylic resin but the fibers were tangled and twisted. The hydrogen

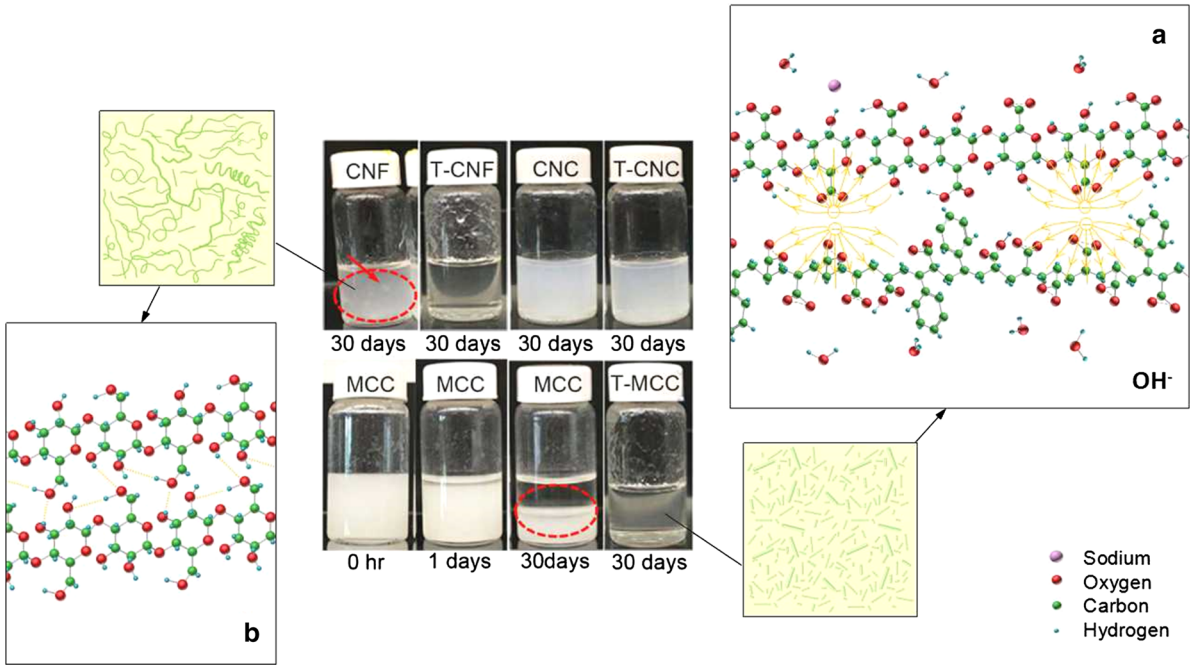

Fig. 8 Stabilizing and dispersing mechanism of original products and oxidized cellulose/acrylic resin dispersions. **a** CNF (0.13 wt%), visual stability of acrylic resin with T-CNF (0.13 wt%), CNC (0.78 wt%), and T-CNC (0.78 wt%), T-MCC (0.78 wt%) dispersions. MCC (0.78 wt%) dispersions were gradually laminated with increased time. **b** The dispersion mechanism of the T-CNPs and acrylic resin dispersions

bonds between the individual CNF also played a role in the aggregation (Fig. 7b). The AR/MCC dispersions maintained a high relative viscosity of the acrylic resin when not stirred for a short time. It progressively deposited with an increase of standing time. Two significant layers of acrylic resin and MCC were observed after 30 days. This might result from the combined effects of the large particle sizes of relative heavy weight, the insufficient surface charge, and the insufficient L/d.

Zeta potentials

As shown in Fig. 9, all three starting cellulose samples bore the negative charges, but the CNC dispersion has the highest negative value of − 67.73 mV and these differences might result from the various complex procedures involved in their productions. The USDA Forest Products Laboratory made the CNCs used in this study from strip-cut prehydrolysis softwood Kraft dissolving pulp via sulfuric acid hydrolysis, which had imparted sulfate anions on the surface of nanocrystals (Reid et al. 2017). The MCC was typically prepared by

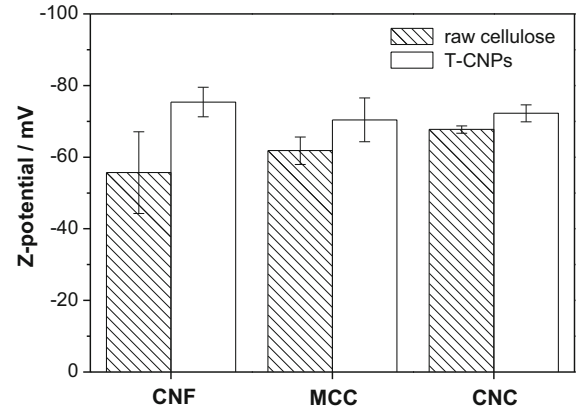

Fig. 9 Various raw cellulose types and the T-CNPs

concentrated acid hydrolysis but not as severe as that used for the preparation of CNCs (Abitbol et al. 2013; Yu et al. 2013), thus having a lower charge than the CNCs. The starting CNFs were made by the University of Maine's Process Development Center with a pilot refining line mechanically disintegrating bleached softwood Kraft pulps. Their negative charges might predominantly be inherited from the Kraft

pulping and bleaching processes (Osterberg et al. 2013). After oxidation, the charges of the resulting T-CNPs increased. The CNFs with a very large L/d exposing more untreated hydroxyl groups readily reacted to produce more carboxyl groups, and thus had slightly higher charges (Sadeghifar et al. 2011; Cho 2010). The observation that the T-CNCs had the lowest carboxyl content (Fig. 2)—but similar charges (Fig. 8)—might indicate that some charges originated from the residual sulfate anions, which were not fully removed during the TEMPO-mediated oxidation.

Steady-flow rheological behaviors

CNP dispersions

The steady-state viscosities of the T-CNP dispersions with concentrations of 0.26, 0.52, 0.78, 1.04, and 1.30 wt% are shown in Fig. 10. The viscosity gradually increased with an increase of the CNP concentration over the entire range of the investigated shear rate and the viscosity generally declined with an increase of the shear rate, demonstrating the shear-thinning behavior of the T-CNP dispersions (Charani et al. 2013).

As shown in Fig. 10a, an increase in the viscosity was observed at a low shear rate and a significant observation was obtained at a high T-CNF concentration, signifying the existence of a network in the uniform T-CNF dispersion that prohibits the shearing at a low shear rate (Chen et al. 2013). A steady decrease in the viscosity was maintained after the shear rate increased to 10^0 s^{-1}. This shear-thinning behavior differed from the four-region shear-thinning behavior of the CNF dispersions that has been reported by Li et al. (2015). The shear-thinning curves are divided into four characteristic regions from 10^{-1} to 10^3 s^{-1}, including a gradual decrease in the viscosity caused by a slow orientation of the CNFs, a plateau resulting from the entangled network, a sharp drop in the viscosity contributed by the breakdown of the entangled network under increased shear force, and a plateau appearing to be the result of the disruption and orientation of most of the entangled network. The TEMPO oxidation resulted in a steady decline in the viscosity owing to the decreased T-CNF L/d with a very small diameter and the well-dispersed T-CNF individuals. This implies that the increased shear force continuously and gradually organized the CNF individuals into a well-oriented structure.

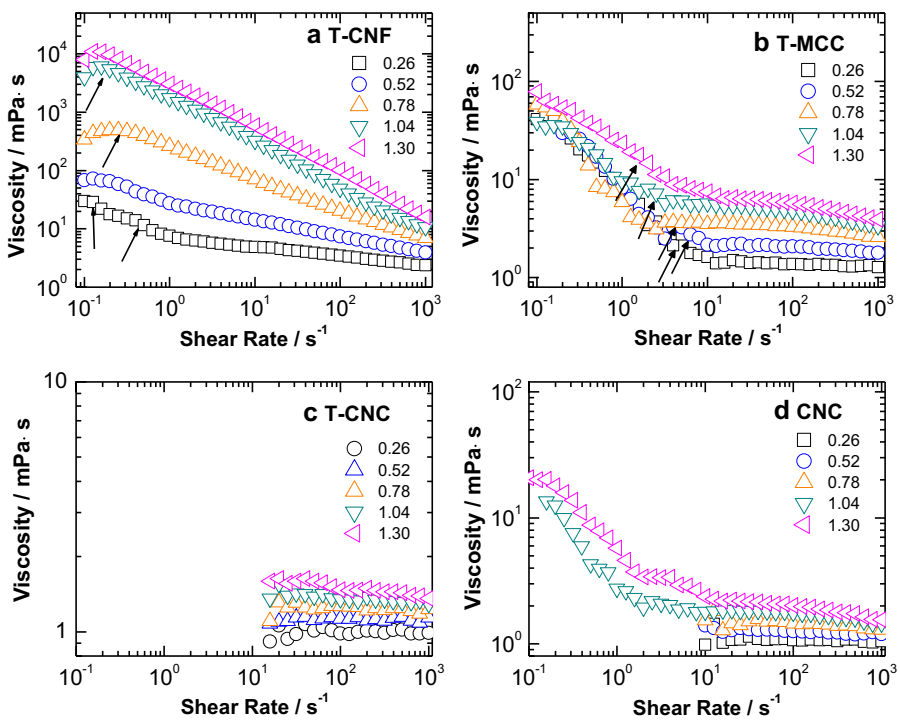

Fig. 10 Steady-state viscosities of the T-CNF, T-MCC, T-CNC, and CNC dispersions with different concentrations at 25 °C. The steady-state viscosities at low concentrations and the low shear rate could not be accurately detected due to the precision of the instrument

The T-MCC suspension exhibited a four-region shear-thinning behavior with the different concentrations except for the suspension with the 1.30 wt%, as shown in Fig. 10b. The T-MCC suspension with 1.30 wt% concentration exhibited a three-region shear-thinning plot, which, in fact, occurred for a similar reason. The L/d was high but lower than the L/d of the T-CNF, resulting in a relatively high viscosity. The shear-thinning behavior dominated the effects at a low shear rate. The T-MCC oriented along the shear direction, causing a decrease of viscosity. As a result of the network caused by the large L/d of the T-MCC and the large particle size, the viscosity reduced the rate of decrease in the shear rate range of 1–8 s^{-1}. With the increase in the shear rate, the shear force broke down the network, leading to a continuous decrease in the viscosity.

The steady-state viscosities were much lower for the T-CNC and CNC dispersions than for the T-CNF and T-MCC dispersions, as shown in Fig. 10c and d. The CNC dispersion exhibited a constant viscosity at a concentration of 0.26 wt% with an increase in the shear rate, which was slightly higher than that of water. This was attributed to the low CNC concentration and the nano-sized particles; the individual CNCs did not prohibit the shearing in the driving direction and exhibited an isotropic structure (Li et al. 2015). The viscosity of CNC dispersions of 0.52 and 0.78 wt% concentration linearly decreased as the shear rate increased from 10 to 10^3 s^{-1}, corresponding to the biphasic structure of the isotropic and liquid crystalline (Li et al. 2015). However, the viscosities of the high concentrations (1.04, 1.3 wt%) declined with an increase in the slope of the shear rate of 10–10^3 s^{-1} and the four-region shear-thinning behavior occurred over the entire range of the shear rate, indicating a crystalline structure. Compared with the CNC dispersion, the T-CNC dispersion with different concentrations exhibited a steady-state viscosity of less than 1.5 mPa s. The plot of the T-CNC dispersion at 0.26 wt% concentration was around 1 mPa s, which was approximately equal to water. The increase in the T-CNC concentration resulted in an increase in the viscosities but showed linear fluctuations, implying that the TEMPO oxidation further reduced the particle size of the CNC (Table 2), resulting in a lack of shear-thinning behavior of the T-CNC dispersion at the investigated concentrations.

In summary, the steady-state viscosities of all CNP dispersions exhibited shear-thinning behavior. However, clear differences were observed as shown in Fig. 10. At the same CNP concentration, the viscosity was higher for the T-CNF dispersion than for the T-MCC and T-CNC dispersions. The T-CNF and T-CNC dispersions exhibited steadily declining viscosity curves with an increase in the shear rate, and T-MCC and CNC showed multi-region shear-thinning behaviors. This resulted from the L/d, particle size, surface charge, and TEMPO oxidation. Compared with the T-CNPs, a high L/d (T-CNF > T-MCC > T-CNC) resulted in high viscosity of the CNP dispersions (Vc: T-CNF > T-MCC > T-CNC). The particle size of the T-CNCs was only half that of the CNCs; therefore, the particle size dominated the decrease in viscosity even when the L/d increased. The TEMPO oxidation also played a role in the decrease in the viscosity of the dispersion. For example, the viscosities of the T-CNC and CNC dispersions were 2.3708 and 1.5061 mPa s, respectively, with concentrations of 1.30 wt% at a shear rate of 10 s^{-1}. At the same concentration, the T-CNC dispersion had a lower viscosity than the CNC dispersion. This was attributed to the TEMPO oxidation shaping the morphology of the CNCs.

AR/T-CNP dispersions

The steady-state viscosities of the AR/T-CNP and AR/CNC dispersions at different concentrations are shown in Fig. 11. These plots indicated that T-CNP and CNC had a clear influence on the steady-state viscosities of the resultant acrylic resins. The acrylic resin itself exhibited a steady plateau over the shear ranges from 0.1 to 10^3 s^{-1}, even with the shear-thickening behavior at the initial shear rate. This is attributable to the fact that the acrylic resin chains overcome the mutual interacting force with the increase of shear rate, forming partials of particle clusters. The viscosity tends to be stable with the equilibration of particle clusters in continuously increasing shear rate. However, the shear-thinning behavior of AR/T-CNP and AR/CNC appeared to be caused by the specific flow performance of the T-CNP or CNC dispersions, significantly changing the steady-state rheological property of the acrylic resin and potentially affecting the subsequent coating process. The viscosity gradually increased with the increase in the CNP

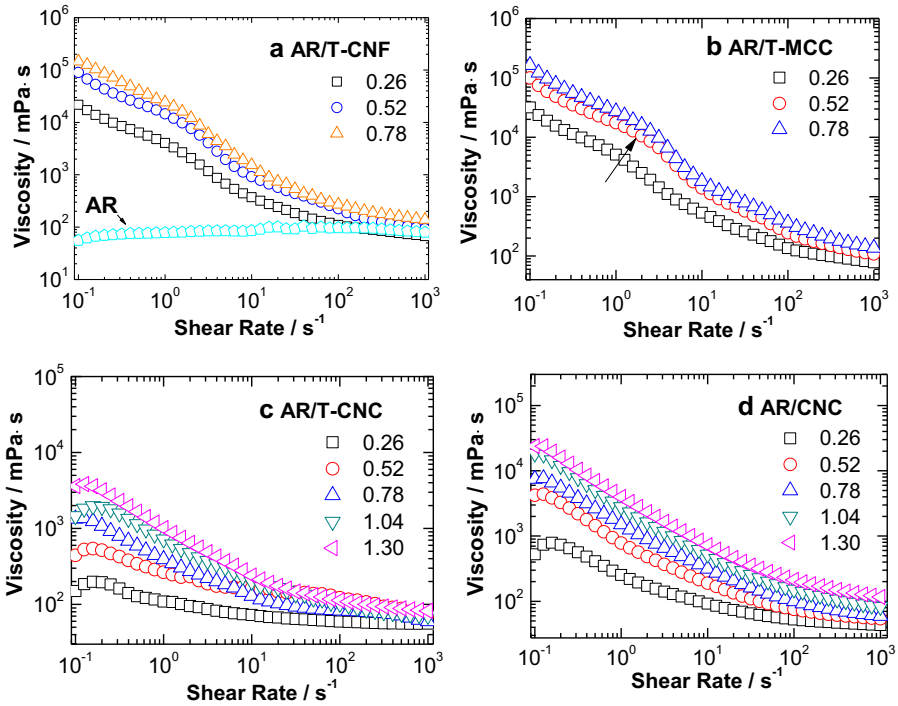

Fig. 11 The steady-state viscosities of the AR/T-CNP and AR/CNC dispersions at different concentrations at 25 °C

concentration over the entire range of the investigated shear rate, and a slow increase was observed when the T-CNP or CNC concentration was greater than 0.78 wt%. The AR/T-CNF and AR/T-MCC dispersions with high concentrations were not able to be prepared in a viscous range because the viscosities of the resultant dispersions at the initial shear rate were greater than 10^2 Pa s with little mobility. As a result, the AR/T-CNF and AR/T-MCC dispersions with high concentrations are not discussed.

The T-CNF dispersions at various concentrations exhibited an almost constant rate of decrease—except at a low shear rate. However, the AR/T-CNF dispersions exhibited a three-region shear-thinning behavior and a plateau near the shear rate of 10^0 s^{-1} at high T-CNF concentrations. This occurred because of the variability of the matrix, water, and acrylic resin. Water was considered a Newtonian fluid with a viscosity of 1.005 mPa s. The shear force is almost equal to the shear rate. A water molecule is far smaller than a T-CNF with a very small inner friction force. When the shear force generated on the dispersion layer by layer, the water molecule prior moved along with the direction of the shear force. The T-CNF interacted with partial of adjacent water molecules, resulting in the shear force acting on the T-CNF, as well. However, the large L/d, the random distribution of the T-CNF, and the insufficient shear force resulted in lagging movement of the T-CNF and some entanglement occurred. Subsequently, the entanglement disappeared parallel to the T-CNF with enhanced shear force. Therefore, only an increase in viscosity was observed at a low shear rate of the T-CNF dispersion. Different from water, the water-based acrylic resin chains were as large as 3–5 nm, and the pure acrylic resin exhibited a high constant viscosity of 84.945 mPa s, denoting a strong shear force caused by the inner friction force generated by the large molecules as compared to water under the same shear rate. The T-CNFs were uniformly dispersed in the acrylic resin with a network-like structure in three-dimensional directions. The increased molecular of matrix lead to the extra-strong force between acrylic resin molecular and T-CNF molecular, generating the three-region shear-thinning behavior. The T-CNF were moved with the acrylic resin chains under the low shear rate as a result of the large inner friction force, while the inner friction force decreased with an increase in the shear rate for the specific flow property of T-CNF dispersion. The T-CNF with a large L/d displayed a different shape

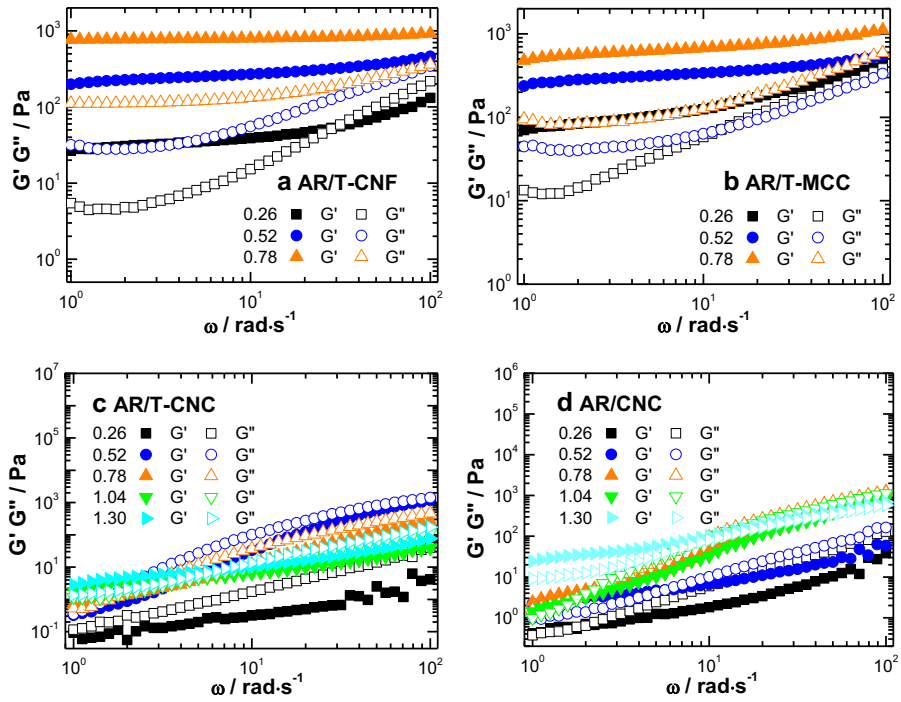

Fig. 12 The storage modulus (G′) and loss modulus (G″) versus angular frequency (ω) of the AR/T-CNP and AR/CNC dispersions at various concentrations

and a random distribution in three-dimensional direction, resulting in forming the entanglement between acrylic resin chains and T-CNF or T-CNF individuals. The entanglement disappeared with the increasing shear rate. As a result, a three-region shear-thinning curve was obtained. The gradual paralleled T-CNF led to a continuous decrease in the viscosity. The AR/T-MCC dispersions exhibited a similar shear-thinning behavior that was attributed to the relative high L/d and large diameter.

The AR/CNC and AR/T-CNC dispersions exhibited a steady decline in the shear-thinning behavior. Compared with the AR/T-CNF and AR/T-MCC dispersions, the viscosity of the AR/CNC and AR/T-CNC dispersions was fairly low. For instance, the viscosities of the acrylic resin dispersions (with T-CNF, T-MCC, T-CNC) were 1896.3, 1830.1, and 129.52 mPa s, respectively at a shear rate of 10 s^{-1} with a T-CNP/CNC concentration of 0.78 wt%, corresponding to the L/d distribution (L/d: T-CNF > T-MCC > T-CNC). A large L/d but smaller particle size resulted in a relative low viscosity, i.e. Vc: AR/T-CNC < AR/CNC, corresponding to the 129.52 < 315.24 mPa s at the 0.78 wt% concentration. This illustrated that the L/d and the particle size were the key parameters affecting the viscosities of the AR/T-CNP or AR/CNC dispersions.

Dynamic rheological behaviors

The dynamic rheological behaviors of the AR/T-CNP dispersions at different T-CNP/CNC concentrations are shown in Fig. 12. An increase in the storage modulus (G′) and the loss modulus (G″) was observed in the angular frequency (ω) range from 1 to 100 s^{-1}. This implied that the viscosity and the elasticity gradually increased over the entire ω range in the T-CNP or CNC concentrations. The network structure caused by the acrylic resin molecule chains in dispersions was continually destroyed and rebuilt in a dynamic balance under the external influence of ω. An increase in the ω affected this dynamic balance, resulting in higher rate of reconstruction than destruction of the network (Wang 2013). As a result, G′ and G″ gradually increased as ω also increased.

As shown in Fig. 12a, at concentrations of 0.26 wt%, the AR/T-CNF dispersions exhibited three types of dynamic rheological behavior over the range of investigated ω, indicating three structures of the dispersions, rigid solid-like, elastic gel-like, and viscous fluid-like. G′ was much higher than G″ when

ω was low, implying a solid-like structure of the resultant dispersions. The gap between G′ and G″ gradually narrowed with the increase in ω indicating the transformation from a solid- to a gel-like structure. When $G' \leq G''$, the dispersions exhibited the performance of a viscous fluid. When the concentration of the T-CNF increased to 0.52 wt%, the resultant dispersions exhibited a solid- and gel-like structure. A steady solid-like structure was obtained at a T-CNF concentration of 0.78 wt%. This was attributed to the increased introduction of inflexible T-CNF, which actually acted as a rigid solid reinforcement. In addition, G′ and G″ increased with increasing T-CNF concentrations. The additional T-CNF had different shapes compared to the acrylic resin molecule chains. These invaders undoubtedly broke the reconstruction and the destruction of the dynamic balance, resulting in variation in the G′ curves. The AR/T-CNF or AR/T-MCC dispersions exhibited similar dynamic rheological behaviors. When $G' > G''$ at a T-MCC concentration of 0.78 wt%, the dynamic rheological behaviors were corresponding with the shear-thinning behavior of steady-state rheological results, implying poor flow property. The G′ of the AR/CNC and AR/T-CNC dispersions was lower than the G″ at low CNC and T-CNC concentrations (0.26, 0.52 wt%), demonstrating a fluid-like structure. G′ was slightly higher than G″ or equal to G″ at high CNC/T-CNC concentrations, resulting in a gel-like structure. As can be understood from Fig. 12c, G′ and G″ gradually increased with increasing concentrations at low values of ω, while G′ and G″ at high concentrations (1.04, 1.30 wt%) were surpassed by the concentrations of 0.78 wt% at high values of ω. One possibility was that a sufficient amount of T-CNC had tiny particle size and were prone to be parallel under the shear force, well participating in the dynamic balance, leading to a slow increase in G′ and G″. Compared with the G′ and G″ of the acrylic dispersions with the same concentration, the AR/CNC and AR/T-CNC dispersions exhibited a relatively low G′ and G″. This demonstrated that even though a rigid solid structure occurred in the acrylic resin, the small particle size and low L/d values still resulted in a fluid-like structure for a certain range of the concentration. The large L/d and the particle size resulted in high G′ and G″ values and a solid-like structure for the AR/T-CNP dispersions.

Conclusions

The TEMPO-oxidized T-CNPs with different particle sizes and L/d ratios were successfully obtained by using a TEMPO/NaBr/NaClO oxidation system. These materials can be well dispersed in aqueous media and the resulting dispersions were transparent. The introduction of carboxyl groups by oxidation reshaped the particles into needle-like structures, reduced the crystallinity, and increased the z-potentials. The AR/T-CNP dispersion showed complete transparency. The T-CNF and T-MCC dispersions exhibited shear-thinning behavior in the investigated concentrations. An increased concentration, large particle size, and high L/d significantly increased the viscosities of the T-CNP dispersions and the resulting AR dispersions. The dispersion of the smaller T-CNC particles did not display the above-mentioned pseudoplastic flow properties in the investigated concentrations. These specific steady-state rheological properties also affected the resultant acrylic resin dispersions. Increases in the L/d or particle size caused the AR/T-CNP dispersions to exhibit various dynamic rheological properties from fluid-like and gel-like structures to solid-like structures. This study demonstrated that the addition of the structural features of cellulose nanoparticles and content T-CNP increased can be tuned to influence the viscosity and flowability of the AR/T-CNP cellulose nanoparticle containing dispersions and decreased their flowability leading to process and/or product improvement.

Acknowledgments This study was supported by the Northwest Advanced Renewables Alliance project sponsored by the National Institute of Food and Agriculture (Grant No. 2011-68005-30416), the National Science Foundation Industry & University Cooperative Research Center for Bioplastics and Biocomposites, and China Scholarship Council.

References

Abitbol T, Kloser E, Gray DG (2013) Estimation of the surface sulfur content of cellulose nanocrystals prepared by sulfuric acid hydrolysis. Cellulose 20:785–794. https://doi.org/10.1007/s10570-013-9871-0

Baldacchini T, Lafratta CN, Farrer RA, Teich MC, Saleh BEA, Naughton MJ et al (2004) Acrylic-based resin with favorable properties for three-dimensional two-photon polymerization. J Appl Phys 95:6072–6076. https://doi.org/10.1063/1.1728296

Benhamou K, Dufresne A, Magnin A, Mortha G, Kaddami H (2014) Control of size and viscoelastic properties of nanofibrillated cellulose from palm tree by varying the tempo-mediated oxidation time. Carbohydr Polym 99:74–83. https://doi.org/10.1016/j.carbpol.2013.08.032

Boluk Y, Zhao L, Incani V (2012) Dispersions of nanocrystalline cellulose in aqueous polymer solutions: structure formation of colloidal rods. Langmuir 28:6114–6123. https://doi.org/10.1021/la2035449

Bousfield D, Richmond F, Bilodeau M (2013) The properties of paper coating layers that contain cellulose nanofibrils. In: TAPPI international conference on nanotechnology for renewable materials, Stockholm, Sweden

Charani PR, Dehghani-Firouzabadi M, Afra E, Shakeri A (2013) Rheological characterization of high concentrated mfc gel from kenaf unbleached pulp. Cellulose 20:727–740. https://doi.org/10.1007/s10570-013-9862-1

Chen P, Yu H, Liu Y, Chen W, Wang X, Ouyang M (2013) Concentration effects on the isolation and dynamic rheological behavior of cellulose nanofibers via ultrasonic processing. Cellulose 20:149–157. https://doi.org/10.1007/s10570-012-9829-7

Cho SY (2010) Flow-induced liquid crystalline solutions prepared from aspect ratio-controlled bacterial cellulose nanowhiskers. Mol Cryst Liq Cryst 519:141–148. https://doi.org/10.1080/15421401003609897

Du L, Wang J, Zhang Y, Qi C, Wolcott MP, Yu Z (2017) A co-production of sugars, lignosulfonates, cellulose, and cellulose nanocrystals from ball-milled woods. Bioresour Technol 238:254–262. https://doi.org/10.1016/j.biortech.2017.03.097

Duan Y, Huo Y, Duan L (2017) Preparation of acrylic resins modified with epoxy resins and their behaviors as binders of waterborne printing ink on plastic film. Colloids and surfaces a: physicochemical and engineering aspects 535:225–231

Elrebii M, Mabrouk AB, Boufi S (2014) Synthesis and properties of hybrid alkyd-acrylic dispersions and their use in VOC-free waterborne coatings. Progress Org Coat 77:757–764. https://doi.org/10.1016/j.porgcoat.2013.12.016

Feng J, Hsieh YL (2013) Chemically and mechanically isolated nanocellulose and their self-assembled structures. Carbohydr Polym 95:32–40. https://doi.org/10.1016/j.carbpol.2013.02.022

French AD (2014) Idealized powder diffraction patterns for cellulose polymorphs. Cellulose 21:885–896. https://doi.org/10.1007/s10570-013-0030-4

Grüneberger F, Künniger T, Zimmermann T, Arnold M (2014) Rheology of nanofibrillated cellulose/acrylate systems for coating applications. Cellulose 21:1313–1326. https://doi.org/10.1007/s10570-014-0248-9

Hay MB, Myneni SCB (2007) Structural environments of carboxyl groups in natural organic molecules from terrestrial systems. Part 1: infrared spectroscopy. Geochim Cosmochim Acta 71:3518–3532. https://doi.org/10.1016/j.gca.2007.03.038

Hunter RJ (1981) Zeta potential in colloids science. Academic Press, New York. https://doi.org/10.1016/b978-0-12-361961-7.50007-9

Jin L, Wei Y, Xu Q, Yao W, Cheng Z (2014) Cellulose nanofibers prepared from tempo-oxidation of kraft pulp and its flocculation effect on kaolin clay. J Appl Polym Sci 131:469–474. https://doi.org/10.1002/app.40450

Kargarzadeh H, Ahmad I, Abdullah I, Dufresne A, Zainudin SY, Sheltami RM (2012) Effects of hydrolysis conditions on the morphology, crystallinity, and thermal stability of cellulose nanocrystals extracted from kenaf bast fibers. Cellulose 19:855–866. https://doi.org/10.1007/s10570-012-9684-6

Li MC, Wu Q, Song K, Lee S, Yan Q, Wu Y (2015) Cellulose nanoparticles: structure–morphology–rheology relationships. ACS Sustain Chem Eng 3:821–832. https://doi.org/10.1021/acssuschemeng.5b00144

Lin L, Shuai Z, Jin Z, Zhen XZ, Hu H, Xin Z et al (2013) Tempo-mediated oxidation of microcrystalline cellulose: influence of temperature and oxidation procedure on yields of water-soluble products and crystal structures of water-insoluble residues. Fibers Polym 14:352–357. https://doi.org/10.1007/s12221-013-0352-8

Moberg T, Sahlin K, Yao K, Geng S, Westman G, Zhou Q et al (2017) Rheological properties of nanocellulose suspensions: effects of fibril/particle dimensions and surface characteristics. Cellulose 24:1–12. https://doi.org/10.1007/s10570-017-1283-0

Okita Y, Saito T, Isogai A (2010) Entire surface oxidation of various cellulose microfibrils by tempo-mediated oxidation. Biomacromolecules 11:1696–1700. https://doi.org/10.1021/bm100214b

Osterberg M, Vartiainen J, Lucenius J, Hippi U, Seppala J, Serimaa R, Laine J (2013) A fast method to produce strong NFC films as a platform for barrier and functional materials. ACS Appl Mater Interfaces 5:4640–4647. https://doi.org/10.1021/am401046x

Reid MS, Villalobos M, Cranston ED (2017) Benchmarking cellulose nanocrystals: from the laboratory to industrial production. Langmuir 33:1583–1598. https://doi.org/10.1021/acs.langmuir.6b03765

Ruiz M, Cavaille J, Dufresne A, Graillat C, Gerard J (2001) New waterborne epoxy coatings based on cellulose nanofillers. Macromol Symp 169:211–222. https://doi.org/10.1002/1521-3900(200105)169:1<211::AID-MASY211>3.0.CO;2-H

Sadeghifar H, Filpponen I, Clarke SP, Brougham DF, Argyropoulos DS (2011) Production of cellulose nanocrystals using hydrobromic acid and click reactions on their surface. J Mater Sci 46:7344–7355. https://doi.org/10.1007/s10853-011-5696-0

Saito T, Isogai A (2004) Tempo-mediated oxidation of native cellulose: the effect of oxidation conditions on chemical and crystal structures of the water-insoluble fractions. Biomacromolecules 5:1983–1989. https://doi.org/10.1021/bm0497769

Sanchez-Garcia MD, Lagaron JM (2010) On the use of plant cellulose nanowhiskers to enhance the barrier properties of polylactic acid. Cellulose 17:987–1004. https://doi.org/10.1007/s10570-010-9430-x

Shibata I, Isogai A (2003) Depolymerization of cellouronic acid during tempo-mediated oxidation. Cellulose 10:151–158. https://doi.org/10.1023/a:1024051514026

Shinoda R, Saito T, Okita Y, Isogai A (2012) Relationship between length and degree of polymerization of tempo-oxidized cellulose nanofibrils. Biomacromolecules 13:842–849. https://doi.org/10.1021/bm2017542

Tan Y, Liu Y, Chen W, Liu Y, Wang Q, Li J et al (2016) Homogeneous dispersion of cellulose nanofibers in waterborne acrylic coatings with improved properties and unreduced transparency. ACS Sustain Chem Eng 4:3766–3772. https://doi.org/10.1021/acssuschemeng.6b00415

Veigel S, Grüll G, Pinkl S, Obersriebnig M, Müller U, Gindl-Altmutter W (2014) Improving the mechanical resistance of waterborne wood coatings by adding cellulose nanofibres. React Funct Polym 85:214–220. https://doi.org/10.1016/j.reactfunctpolym.2014.07.020

Wang L (2013) Dynamic and steady rheological properties of printing pastes and the influence on printing performances. Doctoral dissertation, Donghua University, China

Yu HY, Qin ZY, Liu L, Yang XG, Zhou Y, Yao JM (2013) Comparison of the reinforcing effects for cellulose nanocrystals obtained by sulfuric and hydrochloric acid hydrolysis on the mechanical and thermal properties of bacterial polyester. Compos Sci Technol 87:22–28. https://doi.org/10.1016/j.compscitech.2013.07.024